Acta Cryst. (1996). A52, 909–922

Approximate Methods in Dynamical RHEED Calculations

LIAN-MAO PENG,[a]* S. L. DUDAREV[b] AND M. J. WHELAN[b]

[a]*Beijing Laboratory of Electron Microscopy, Chinese Academy of Sciences, PO Box 2724, Beijing 100080, People's Republic of China, and* [b]*Department of Materials, University of Oxford, Parks Road, Oxford OX1 3PH, England. E-mail: lmpeng@lmplab.blem.ac.cn*

(Received 1 February 1996; accepted 17 June 1996)

Abstract

Approximate methods have been examined in the context of dynamical reflection high-energy electron diffraction (RHEED) calculations using two-dimensional Bloch waves. These approximate methods include Bethe potentials, the utilization of the block structure of the scattering matrix and the perturbation treatment of anomalous absorption effects. It is shown that the use of Bethe potentials provides a very efficient and accurate means for dealing with evanescent waves and numerical examples show that the use of Bethe potentials speeds up the calculations typically more than 15 times. The other two methods examined are less powerful and the improvement in computation efficiency varies from 30 to 60%. It is found that in general the perturbation method for dealing with anomalous absorption effects does not work with high precision.

1. Introduction

The technique of reflection high-energy electron diffraction (RHEED) utilizes high-energy electrons (roughly from 10 to 100 keV) and small-angle diffraction geometry. The latter makes it an ideal technique for combination with molecular-beam epitaxial (MBE) growth techniques for surface and growth studies (Larsen & Dobson, 1988; Cohen & Ichimiya, 1993). The use of high-energy electrons, on the other hand, simplifies the theoretical treatment of the diffraction processes. This is because for high-energy electron diffraction the complicated exchange and correlation effects (see, for example, Pendry, 1974) are negligible and the movement of high-energy electrons in a solid is basically governed by the electrostatic potential between the high-energy electrons and the electrons and nuclei of the solid.

Various methods have been proposed for calculating dynamical RHEED intensities and analysing experimental diffraction data (Maksym & Beeby, 1981; Ichimiya, 1983; Peng & Cowley, 1986, 1988; Zhao, Poon & Tong, 1988; Smith & Lynch, 1988; Meyer-Ehmsen, 1989; Peng & Whelan, 1990). Formally, it can be shown that these different methods are equivalent. A round-robin exercise of RHEED calculations has also been organized by Professor A. Ichimiya in order to compare numerical results from major groups around the world. The first exercise revealed that the results of Dudarev, Korte, Maksym and Peng are nearly identical (Ichimiya, 1996). A second exercise is under way in order to determine the origin of discrepancies between calculations by these authors and other groups.

All RHEED theories, except the one by Peng & Cowley (1986, 1988), divide the crystal into slices parallel to the surface. With the assumption of a two-dimensional periodicity of the crystal parallel to the surface, the task of performing dynamical RHEED calculations is then reduced to a problem of solving a set of second-order differential equations (Tournarie, 1962). These second-order differential equations can be transformed into first-order coupled differential and integral equations (Maksym & Beeby, 1981) or simply into first-order non-linear differential equations (Meyer-Ehmsen, 1989; Dudarev & Whelan, 1994) and numerical routines are available for solving these first-order differential equations. Alternatively, dynamical RHEED theory can be formulated as an eigenvalue problem (Lynch & Moodie, 1972; Ichimiya, 1983; Zhao *et al.*, 1988; Peng & Whelan, 1990).

The dependence of dynamical RHEED calculations on the number of beams used has been examined by Zhao & Tong (1988). These authors emphasized the importance of both the propagating and the evanescent higher-order Laue-zone (HOLZ) beams in dynamical RHEED calculations, and concluded that to achieve a convergent result 60 rods are needed for simple unreconstructed surfaces. For more complicated reconstructed surfaces, this requirement excludes most researchers from performing reliable dynamical RHEED calculations except those who have access to supercomputers.

It is the aim of this paper to examine some approximate methods and their implications for dynamical RHEED calculations. In particular, we focus our attention on the so-called Bethe-potentials method, by which the number of rods that need to be included in RHEED calculations can be substantially reduced. We found that the incorporation of Bethe potentials (Bethe, 1928) in our Bloch-wave approach improves the computation efficiency typically more than 15 times. In a separate paper (Peng, Dudarev & Whelan, 1996), we have shown that the use of Bethe potentials not only speeds up numerical computations but also leads to a

convergent method for dynamical RHEED calculation from the surface of a semi-infinite crystal.

In some theories of RHEED, the effect of absorption has been treated using a perturbation method, see *e.g.* Ichimiya (1983). In this paper, we will show that, although the perturbation treatment of absorption effects speeds up the calculations typically by 30%, this method is not very accurate. Some discrepancies found during the first round robin of RHEED calculations may result from the use of the perturbation treatment of the absorption effects. In this paper, we have also examined the use of the block structure of the scattering matrix for a reconstructed surface. For a simple Si (001) 2×1 surface, we found the method speeds up computation typically by 60%. For more complicated surfaces, such as the Si (111) 7×7 and GaAs (110) 2×4 surfaces, further improvement in the computation efficiency may be expected.

2. Basic relations and two-dimensional Bloch waves

Following Bethe (1928), we start our discussion from the well known dispersion equation of the dynamical theory of electron diffraction

$$[K^2 - (\mathbf{k} + \mathbf{g})^2]C_g + \sum_{h \neq g} U_{g-h} C_h = 0, \qquad (1)$$

where $\mathbf{K}$ is the electron wave vector derived from the incident electron wave vector χ after correction for the mean inner potential, *i.e.* $K^2 = \chi^2 + U_0$. U_g and C_g are defined respectively by the Fourier and Bloch-function expansions of the crystal potential

$$U(\mathbf{r}) = \sum_g U_g \exp(i\mathbf{g} \cdot \mathbf{r}), \qquad (2)$$

and wave function

$$\psi(\mathbf{r}) = \sum_g C_g \exp[i(\mathbf{k} + \mathbf{g}) \cdot \mathbf{r}], \qquad (3)$$

where $\mathbf{g}$ denotes a vector of the three-dimensional reciprocal lattice.

By introducing a parameter γ defined by

$$\mathbf{k} = \mathbf{K} + \gamma \mathbf{n}, \qquad (4)$$

where $\mathbf{n}$ is a unit vector pointing toward the crystal (along the positive z direction), the dispersion equations (1) can be reduced to

$$[\gamma^2 + 2(\mathbf{K} + \mathbf{g})_z \gamma - 2Ks_g]C_g - \sum_{h \neq g} U_{g-h} C_h = 0, \qquad (5)$$

where s_g is the excitation error for reflection $\mathbf{g}$ given by

$$s_g = [K^2 - (\mathbf{K} + \mathbf{g})^2]/2K. \qquad (6)$$

In RHEED, an incident beam of electrons, typically of order 10 to 100 keV, is incident at a surface of a crystal at a glancing angle of a few degrees. The arrangement of atoms in the surface region may differ from that in the bulk. In general, the surface structure is two-dimensionally periodic in the plane parallel to the surface. The potential variation along the surface normal or z direction is modelled by dividing the crystal into many thin slices parallel to the surface, and assuming that within each slice the potential is two-dimensionally periodic parallel to the surface and constant normal to the surface. Since the potential field in each slice is constant along the z direction, only zero-order Laue-zone (ZOLZ) reflections with $g_z = 0$ need to be included in (2) and (3). If the two-dimensional reciprocal-lattice vectors of the surface periodicity are denoted by $\mathbf{G} = (G_x; G_y)$, then within a thin slice situated at coordinate z (1) leads directly to

$$\{(\gamma + K_z)^2 - [K^2 - (\mathbf{K}_t + \mathbf{G})^2]\}C_G - \sum_{H \neq G} U_{G-H}(z) C_H = 0, \qquad (7)$$

in which the subscript t denotes the tangential component $\mathbf{K}_t = (K_x; K_y)$ of $\mathbf{K}$ in the plane parallel to the surface. By the introduction of two new parameters

$$\mathcal{K} = \gamma + K_z; \quad \Gamma_G^2 = K^2 - (\mathbf{K}_t + \mathbf{G})^2,$$

(7) can be expressed as

$$(\mathcal{K}^2 - \Gamma_G^2)C_G - \sum_{H \neq G} U_{G-H}(z) C_H = 0. \qquad (8)$$

This equation is an eigenvalue equation for $\mathcal{K}^2$. If n reciprocal-lattice rods are included, this equation will yield $2n$ distinct eigenvalues

$$\mathcal{K}^{(1)}, \mathcal{K}^{(2)}, \ldots, \mathcal{K}^{(n)}, -\mathcal{K}^{(1)}, -\mathcal{K}^{(2)}, \ldots, -\mathcal{K}^{(n)},$$

n independent eigenvectors $C_G^{(i)}$ $(i = 1, \ldots, n)$ and $2n$ distinct two-dimensional Bloch waves

$$b^{(j)}(\mathbf{x}, z) = \sum_G C_G^{(j)} \exp[i(\mathbf{K}_t + \mathbf{G}) \cdot \mathbf{x} + i\mathcal{K}^{(j)} z], \qquad (9)$$

where we have used the notation $\mathbf{r} = (\mathbf{x}, z)$.

3. The optical potential

For a three-dimensional periodic potential, the Fourier coefficients of the scaled potential $U(\mathbf{r})$ that appear in (1) are given by

$$U_g = (4\pi/V_c)(m/m_0) \sum_i f_i(s) \exp(-B_i s^2) \exp(-i\mathbf{g} \cdot \mathbf{r}_i), \qquad (10)$$

in which V_c is the volume of the crystal unit cell, $f_i(g)$ is the atomic scattering factor for the ith atom, the

summation over i is taken over all atoms within the unit cell, B is the usual Debye–Waller factor and $s = g/(4\pi)$. For a recent tabulation of the Debye–Waller factors of elemental crystals, see Peng, Ren, Dudarev & Whelan (1996*a*).

The effects of inelastic scattering upon the elastically scattered electrons may be represented by regarding the interaction potential between the incident electron and the crystal as being complex. For high-energy electron diffraction and to a good approximation, the collective electronic excitations contribute mainly to the imaginary part of the mean inner potential U_0 (Yoshioka, 1957; Whelan, 1965*a*), while the dominant contributions to the imaginary part of all other U_g come from thermal diffuse scattering (TDS) (Yoshioka & Kainuma, 1962; Whelan, 1965*b*; Hall & Hirsch, 1965; Bird & King, 1990). In our calculations, the mean absorption is treated as a free parameter, and when appropriate Radi's (1970) values are used. The complex Fourier coefficients U_g for all other reflections are calculated using the parameterization procedure of Dudarev, Peng & Whelan (1995) and Peng, Ren, Dudarev & Whelan (1996*a*,*b*), in which both the real and the imaginary parts of the scattering factors have been approximated using a set of fitting parameters a_i and b_i as follows:

$$f(s) = \sum_{i=1}^{n} a_i \exp(-b_i s^2). \tag{11}$$

It should be noted that the coefficients tabulated in Peng *et al.* (1996*a*) were calculated for 100 keV electrons. For any other primary-beam energy E, these coefficients can be converted appropriately using the formula given in Peng *et al.* (1996*a*,*b*).

The variation with z of the two-dimensional Fourier coefficients $U_G(z)$ is calculated from the Fourier series

$$U_G(z) = \sum_{g_z} U_{G,g_z} \exp(ig_z z). \tag{12}$$

To model the potential variation across the selvedge where only the two-dimensional periodicity parallel to the surface remains, we construct an artificial unit cell having a large dimension normal to the surface. To illustrate this procedure, we consider the case of an Ag(001) surface as an example. Ag has the f.c.c. structure with lattice constant $a_0 = 4.09$ Å and four atoms within the conventional unit cell. The fractional atomic coordinates for the four atoms are: $(0, 0, 1/4)$, $(1/2, 1/2, 1/4)$, $(1/2, 0, 3/4)$ and $(0, 1/2, 3/4)$. To simulate the potential variation from the substrate to the vacuum, a large unit cell with the following lattice parameters is constructed: $a = a_0$, $b = a_0$, $c = 4a_0$. Eight Ag atoms are placed in the large unit cell, with fractional atomic coordinates: $(0, 0, 5/16)$, $(1/2, 1/2, 5/16)$, $(1/2, 0, 7/16)$, $(0, 1/2, 7/16)$, $(0, 0, 9/16)$, $(1/2, 1/2, 9/16)$, $(1/2, 0, 11/16)$ and

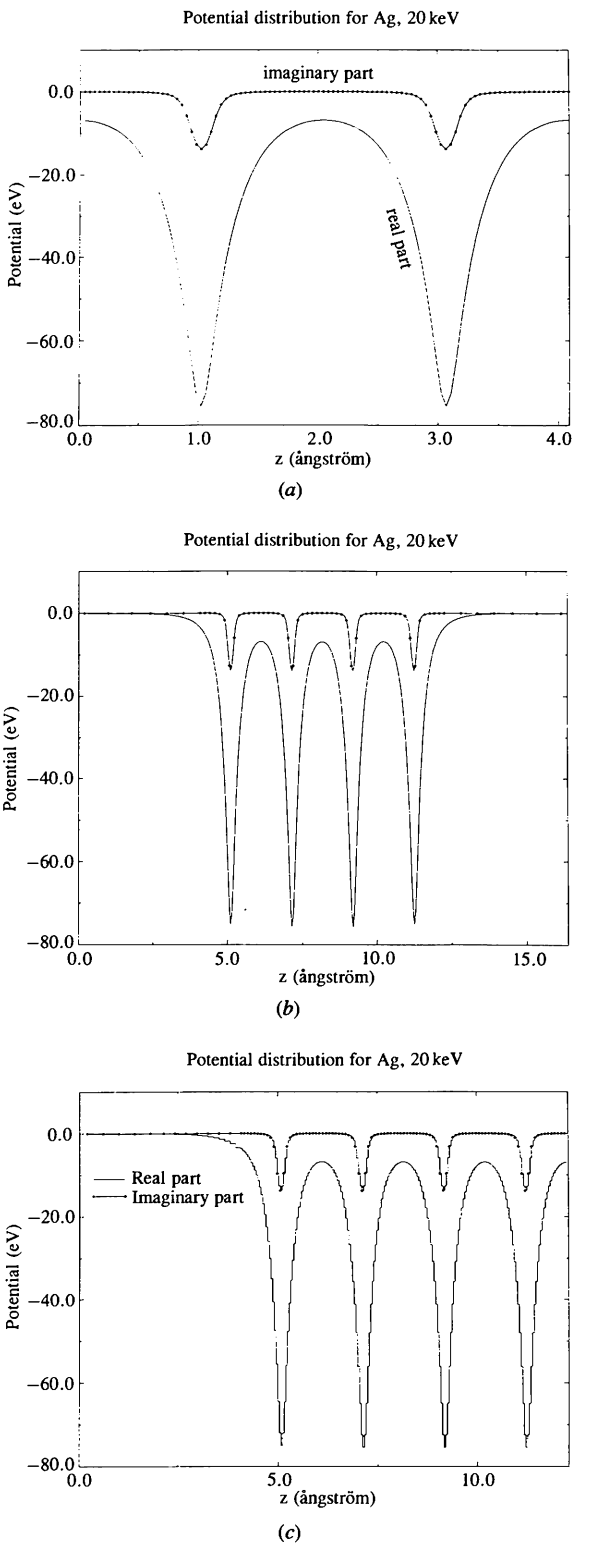

Fig. 1. Real and imaginary parts of the optical potential $U_0(z)$ for (*a*) a perfect bulk Ag single-crystal unit cell, (*b*) the artificial large unit cell described in the text and (*c*) the combination of (*a*) and (*b*) to simulate the selvedge. The z direction is along $[00\bar{1}]$ and the incident-beam energy is 20 keV.

$(0, 1/2, 11/16)$. Fig. 1 shows $U_0(z)$ (*a*) for the perfect bulk Ag single crystal and (*b*) for the artificial crystal with the large unit cell. It is seen from Fig. 1(*b*) that near the middle of the unit cell the potential is very close to the bulk value of Fig. 1(*a*). On the other hand, to the left of Fig. 1(*b*), a smooth potential variation from free space to the crystal is clearly reproduced. By combining half the curve of Fig. 1(*b*) with the bulk curve of Fig. 1(*a*), we then obtain the potential (Fig. 1*c*) that is appropriate for dynamical RHEED calculations. It should be noted that in Fig. 1(*c*) the continuously varying potential has been replaced by a stepped function in accordance with the assumption from which (7) and (8) are derived and that a variable sampling rate over the potential distribution is possible, as can be seen in Fig. 1(*c*).

Alternatively, $U_G(z)$ can be calculated explicitly using the fitting parameters a_i and b_i (see, for example, Appendix *B* of Peng, 1994):

$$\begin{aligned} V_G(z) = (4\pi\hbar^2/S_0 m_0) \sum_{n,i} \exp(-i\mathbf{G}\cdot\mathbf{x}_n) \\ \times \{a_{i,n}^{(\mathrm{Re})}[\pi/(b_{i,n}^{(\mathrm{Re})} + B_n)]^{1/2} \\ \times \exp[-(b_{i,n}^{(\mathrm{Re})} + B_n)G^2/(4\pi)^2 \\ - 4\pi^2(z - z_n)^2/(b_{i,n}^{(\mathrm{Re})} + B_n)] \\ + i a_{i,n}^{(\mathrm{Im})}[\pi/(b_{i,n}^{(\mathrm{Im})} + B_n)]^{1/2} \\ \times \exp[-(b_{i,n}^{(\mathrm{Im})} + B_n)G^2/(4\pi)^2 \\ - 4\pi^2(z - z_n)^2/(b_{i,n}^{(\mathrm{Im})} + B_n)]\}, \end{aligned} \tag{13}$$

in which the summation over n is carried out over all atoms belonging to a surface unit cell and S_0 denotes the area of the unit cell.

4. Dynamical RHEED calculations using two-dimensional Bloch waves

In terms of two-dimensional Bloch waves, the total wave function within a slice that has a constant potential normal to the surface is given by

$$\begin{aligned} \psi(\mathbf{r}) &= \sum_{j=1}^{2n} \alpha^{(j)} b^{(j)}(\mathbf{x}, z) \\ &= \exp(i\mathbf{K}_t\cdot\mathbf{x}) \sum_G \psi_G(z) \exp(i\mathbf{G}\cdot\mathbf{x}), \end{aligned} \tag{14}$$

where $\alpha^{(j)}$ is the Bloch-wave excitation amplitude of the jth Bloch wave and $\psi_G(z)$ is the diffracted-beam amplitude associated with the Gth rod of the reciprocal lattice and is given by

$$\psi_G(z) = \sum_{j=1}^{2n} \alpha^{(j)} C_G^{(j)} \exp(i\mathcal{K}^{(j)} z). \tag{15}$$

The first-order surface-normal derivative of $\psi_G(z)$ is given by

$$\psi'_G(z) = i \sum_{j=1}^{2n} \alpha^{(j)} \mathcal{K}^{(j)} C_G^{(j)} \exp(i\mathcal{K}^{(j)} z). \tag{16}$$

We now define a vector $\boldsymbol{\Psi}$ as follows:

$$\begin{aligned} \boldsymbol{\Psi}(z) &= \begin{pmatrix} \{\psi_G(z)\} \\ \{-i\psi'_G(z)\} \end{pmatrix} \\ &= \begin{pmatrix} \left\{ \sum_{j=1}^{2n} \alpha^{(j)} C_G^{(j)} \exp(i\mathcal{K}^{(j)} z) \right\} \\ \left\{ \sum_{j=1}^{2n} \alpha^{(j)} \mathcal{K}^{(j)} C_G^{(j)} \exp(i\mathcal{K}^{(j)} z) \right\} \end{pmatrix}. \end{aligned} \tag{17}$$

In matrix notation, the above expression can be written in a more compact form (Peng & Whelan, 1990):

$$\boldsymbol{\Psi}(z) = \mathbf{C}\boldsymbol{\Upsilon}(z)\boldsymbol{\alpha}, \tag{18}$$

where $\boldsymbol{\Upsilon}(z)$ is a $2n \times 2n$ diagonal matrix with $\{\Upsilon\}_{i,i} = \exp(i\mathcal{K}^{(i)} z)$, $\{\Upsilon\}_{i+n,i+n} = \exp(-i\mathcal{K}^{(i)} z)$ $(i = 1, \ldots, n)$ and

$$\mathbf{C} = \begin{pmatrix} \{C_G^{(i)}\} & \{C_G^{(i)}\} \\ \{\mathcal{K}^{(i)} C_G^{(i)}\} & \{-\mathcal{K}^{(i)} C_G^{(i)}\} \end{pmatrix}$$

is a general $2n \times 2n$ matrix and $\boldsymbol{\alpha}$ is a $2n$-dimensional vector with elements $\{\alpha\}_i = \alpha^{(i)}$.

If z_t and z_b are the coordinates of the top and bottom surfaces of the slice, then from (18) we have

$$\boldsymbol{\Psi}(z_t) = \mathbf{C}\boldsymbol{\Upsilon}(z_t)\boldsymbol{\alpha},$$

which gives

$$\boldsymbol{\alpha} = \boldsymbol{\Upsilon}(-z_t)\mathbf{C}^{-1}\boldsymbol{\Psi}(z_t). \tag{19}$$

Substituting (19) into (18), we obtain an expression relating the vectors $\boldsymbol{\Psi}$ at the top and bottom surfaces of a thin slice:

$$\boldsymbol{\Psi}(z_b) = \mathbf{M}\boldsymbol{\Psi}(z_t), \tag{20}$$

in which the matrix $\mathbf{M}$ is called the scattering matrix following the convention of high-energy electron diffraction (Sturkey, 1962). If we use a set of integers k to index the thin slices, the scattering matrix for the kth thin slice is given by

$$\mathbf{M}_k(t_k) = \mathbf{C}_k\boldsymbol{\Upsilon}_k(t_k)\mathbf{C}_k^{-1}, \tag{21}$$

t_k being the thickness of the kth slice.

We now consider a general diffraction problem as shown schematically in Fig. 2. Since the vacuum region above the upper surface contains only the incident and

reflected beams, the wave function will be of the form

$$\Psi^{v}_{\text{upper}}(\mathbf{r}) = \sum_G \{\mathcal{I}_G^+ \exp(ik_{G,z}z) + \mathcal{R}_G \exp(-ik_{G,z}z)\} \times \exp(i\mathbf{k}_{G,t}\cdot\mathbf{x}), \quad (22)$$

in which $\mathcal{I}_G^+$ and $\mathcal{R}_G$ represent the incident- and the reflected-beam amplitudes associated with the Gth reciprocal-lattice rod, respectively.

At the upper surface ($z = 0$), where the origin lies, we have

$$\Psi(0) = \begin{pmatrix} \{\psi_G(0)\} \\ \{-i\psi'_G(0)\} \end{pmatrix} = \begin{pmatrix} \{\mathcal{I}_G^+ + \mathcal{R}_G\} \\ \{k_{G,z}(\mathcal{I}_G^+ - \mathcal{R}_G)\} \end{pmatrix} = \begin{pmatrix} \mathbf{I}^+ + \mathbf{R} \\ \mathbf{P}(\mathbf{I}^+ - \mathbf{R}) \end{pmatrix},$$

where the matrix $\mathbf{P}$ is a diagonal matrix with $P_{GG} = k_{G,z}$.

In the vacuum region below the lower face of the last slice, the wave function is given by

$$\Psi^{v}_{\text{lower}}(\mathbf{r}) = \sum_G \{\mathcal{I}_G^- \exp(-ik_{G,z}z) + \mathcal{T}_G \exp(ik_{G,z}z)\} \times \exp[i(\mathbf{k}_{G,t}\cdot\mathbf{r})], \quad (23)$$

where $\mathcal{I}_G^-$ and $\mathcal{T}_G$ are the Gth incident- and reflected-beam amplitudes from below the crystal slab, respectively. At the exit face,

$$\Psi(t) = \begin{pmatrix} \{\psi_G(t)\} \\ \{-i\psi'_G(t)\} \end{pmatrix} = \begin{pmatrix} \mathbf{QT} + \mathbf{Q}^{-1}\mathbf{I}^- \\ \mathbf{P}(\mathbf{QT} - \mathbf{Q}^{-1}\mathbf{I}^-) \end{pmatrix},$$

in which $\mathbf{Q}$ is a diagonal matrix with $Q_{GG} = \exp(ik_{G,z}t)$.

The wave vectors of the reflected beams are given by

$$\mathbf{k}_{G,t} = \chi_t + \mathbf{G}; \quad \mathbf{k}_{G,z} = -\mathbf{n}(\chi^2 - \mathbf{k}_{G,t}^2)^{1/2}. \quad (24)$$

The reflected-beam amplitudes $\{\mathcal{F}_G\}$ can be calculated for $\mathbf{I}^- = 0$ by propagating an $\mathbf{R}$ matrix relating $\{\psi_G(z)\}$ and $\{\psi'_G(z)\}$ through the crystal (Ichimiya, 1983; Zhao *et al.*, 1988). Assuming our model system consists of a total of m repeating bulk unit slabs and the selvedge, then starting from the bottom face of the bulk slab, we have

$$\Psi(z_{m-1}) = \begin{pmatrix} \mathbf{M}_{11} & \mathbf{M}_{12} \\ \mathbf{M}_{21} & \mathbf{M}_{22} \end{pmatrix}_m^{-1} \begin{pmatrix} \mathbf{Q}(t)\mathbf{T} \\ \mathbf{PQ}(t)\mathbf{T} \end{pmatrix} = \begin{pmatrix} \mathbf{M}'_{11} + \mathbf{M}'_{12}\mathbf{P} \\ \mathbf{M}'_{21} + \mathbf{M}'_{22}\mathbf{P} \end{pmatrix}_m (\mathbf{Q}(t)\mathbf{T}), \quad (25)$$

where

$$\mathbf{M}'_m = \mathbf{M}_m^{-1} = \mathbf{C}_m \Upsilon(-t_m)\mathbf{C}_m^{-1}. \quad (26)$$

Letting

$$\mathbf{R}_m = (\mathbf{M}'_{21} + \mathbf{M}'_{22}\mathbf{P})_m(\mathbf{M}'_{11} + \mathbf{M}'_{12}\mathbf{P})_m^{-1}, \quad (27)$$

we obtain from (25)

$$\{-i\psi'_G\}_{m-1} = \mathbf{R}_m\{\psi_G\}_{m-1}, \quad (28)$$

where $\mathbf{R}_m$ is the $\mathbf{R}$ matrix of the mth layer.

The $\mathbf{R}$ matrix can be propagated upward through the bulk crystal slab composed of repeating unit slabs with indices $i = m-1, \ldots, 1$. Defining the $\mathbf{R}$ matrix generally by

$$\{-i\psi'_G(z)\}_i = \mathbf{R}_{i+1}\{\psi_G(z)\}_i, \quad (29)$$

we have for the ith unit slab

$$\Psi(z_{i-1}) = \begin{pmatrix} \mathbf{M}'_{11} & \mathbf{M}'_{12} \\ \mathbf{M}'_{21} & \mathbf{M}'_{22} \end{pmatrix}_i \begin{pmatrix} \{\psi_G\} \\ \{-i\psi'_G\} \end{pmatrix}_i = \begin{pmatrix} \mathbf{M}'_{11} & \mathbf{M}'_{12} \\ \mathbf{M}'_{21} & \mathbf{M}'_{22} \end{pmatrix}_i \begin{pmatrix} \mathbf{I} \\ \mathbf{R}_{i+1} \end{pmatrix} \{\psi_G\}_i, \quad (30)$$

in which $\mathbf{I}$ is the usual unit matrix. Equation (30) gives the recurrence relation

$$\mathbf{R}_i = [(\mathbf{M}'_{21})_i + (\mathbf{M}'_{22})_i\mathbf{R}_{i+1}][(\mathbf{M}'_{11})_i + (\mathbf{M}'_{12})_i\mathbf{R}_{i+1}]^{-1}. \quad (31)$$

At the selvedge/substrate interface, we have

$$\begin{pmatrix} \mathbf{I}^+ + \mathbf{R} \\ \mathbf{P}(\mathbf{I}^+ - \mathbf{R}) \end{pmatrix} = \begin{pmatrix} \mathbf{M}'_{11} & \mathbf{M}'_{12} \\ \mathbf{M}'_{21} & \mathbf{M}'_{22} \end{pmatrix}_s \begin{pmatrix} \mathbf{I} \\ \mathbf{R}_1 \end{pmatrix} \{\psi_G\}_0 = \begin{pmatrix} \mathbf{S}_1 \\ \mathbf{S}_2 \end{pmatrix} \{\psi_G\}_0, \quad (32)$$

where the subscript s denotes selvedge matrices and

$$\mathbf{S}_1 = (\mathbf{M}'_{11})_s + (\mathbf{M}'_{12})_s\mathbf{R}_1,$$
$$\mathbf{S}_2 = (\mathbf{M}'_{21})_s + (\mathbf{M}'_{22})_s\mathbf{R}_1.$$

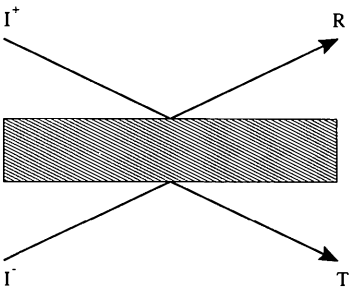

Fig. 2. Schematic diagram showing the diffraction geometry where the column vectors $\mathbf{I}^+$ and $\mathbf{I}^-$ are incident on the crystal slab from above and below the slab and are reflected giving column vectors $\mathbf{R}$ and $\mathbf{T}$ for the top and bottom faces of the slab, respectively.

After some manipulation, we obtain from (32):

$$\mathbf{R} = -(\mathbf{S}_1^{-1} + \mathbf{S}_2^{-1}\mathbf{P})^{-1} \cdot (\mathbf{S}_1^{-1} - \mathbf{S}_2^{-1}\mathbf{P})\mathbf{I}^+. \quad (33)$$

When evanescent waves with large imaginary components of $\mathcal{K}^{(i)}$ are present, the scattering matrix for even a single unit slab or the selvedge may diverge. In this case, both the selvedge and the bulk unit slab need to be divided into several subslabs and the propagation of the **R** matrix through these subslabs follows exactly the same procedure as described by (30)–(31).

We now consider the calculation of dynamical RHEED from an Ag(001) surface using (33). This is the system originally considered by Maksym & Beeby (1981). To avoid confusion, we will follow their indexing system and call all reflections (H, K) with non-zero negative-K-value higher-order Laue-zone (HOLZ) reflections and all reflections with non-zero positive-K-value minus HOLZ (MHOLZ) reflections. All reflections having indices of the form $(H, 0)$ are called zero-order Laue-zone (ZOLZ) reflections. The high-energy electrons are incident on the (001) surface along the [01] direction, which corresponds to the conventional [110] azimuth. In this paper, with the exception of Fig. 3, we choose to plot the quantity $|\mathcal{R}_G|$ rather than the experimentally measurable quantity $|\mathcal{R}_G|^2 \,\mathrm{Re}(k_{G_z}/k_{0_z})$, in which G and 0 refer to the incident and reflected beams, respectively.

Shown in Fig. 3 are two sets of curves $|\mathcal{R}_G|$ and $|\mathcal{R}_G|^2 \,\mathrm{Re}(k_{G_z}/k_{0_z})$. For simplicity in subsequent discussion, we will refer to the former type of curve as an amplitude plot and the latter type as a rocking curve. The curves were calculated for 20 keV using 16 rods: $(0,0)$, $(\pm1,0)$, $(\pm2,0)$, $(\pm3,0)$, $(\pm4,0)$, $(0,1)$, $(\pm1,1)$, $(\pm2,1)$, $(\pm3,1)$. Shown in Fig. 3(*a*) are plots for the $(0,0)$ rod and in Fig. 3(*b*) plots for the $(1,0)$ rod. The major differences between the two curves are that in the amplitude plot the weak peaks are more pronounced than in the rocking curve and that in the amplitude plot even the evanescent beam is recorded. For example, for the $(1,0)$ beam (Fig. 3*b*), for angles of incidence smaller than about 29 mrad, k_{G_z} is pure imaginary, *i.e.* the beam is evanescent. This beam is therefore invisible in the usual rocking curve for $\theta < 29$ mrad. Since in the present study we do not intend to compare our results with experimental observations and since conversion between these two types of curve can be readily made, we choose to use the amplitude plot rather than the rocking curve.

Having calculated the reflected-beam amplitudes $\mathcal{R}_G$, the calculation of the electron wave function can then be performed using the two-dimensional Bloch-wave approach. In the vacuum region above the surface, the wave function is given by (22) while in the crystal it is given by (14). The wave function in the selvedge and within the substrate can be obtained by propagating the vector Ψ downward through the assemblage of thin slices with indices $i = 1, 2, \ldots$. At the vacuum/selvedge interface, we have

$$\begin{pmatrix} \{\psi_G(z)\} \\ \{-i\psi'_G(z)\} \end{pmatrix}_1 = \mathbf{M}_1(z) \begin{pmatrix} \mathbf{I}^+ + \mathbf{R} \\ \mathbf{P}(\mathbf{I}^+ - \mathbf{R}) \end{pmatrix}, \quad (34)$$

and, in the crystal,

$$\Psi_{k+1}(z) = \mathbf{M}_k(t_k)\Psi_k(z). \quad (35)$$

It should be noted that the scattering matrix $\mathbf{M}_k$ for all thin slices have already been calculated in the process of calculating $\mathcal{R}_G$. In the present scheme, the calculation of the electron wave function therefore does not require much extra effort, except for multiplication of some $2n \times 2n$ matrices.

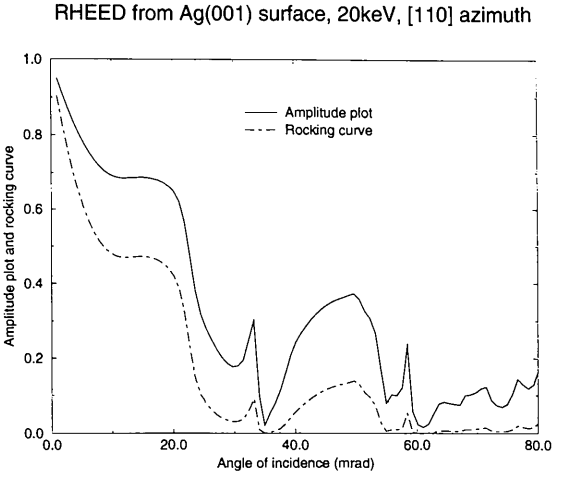

(*a*)

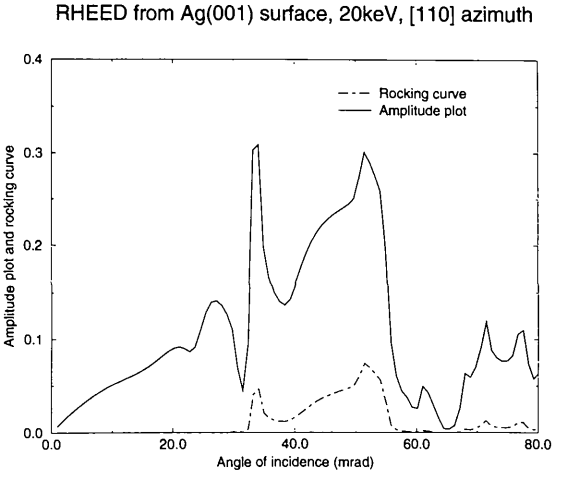

(*b*)

Fig. 3. Amplitude plot and rocking curves for (*a*) (00) rod and (*b*) (10) rod. The curves are calculated for 20 keV incident-beam energy using 16 rods.

Shown in Fig. 4 are distributions of $|\psi_G(z)|^2$ for the (00) and (10) rods, and for an angle of incidence of (*a*) $\theta = 14$ mrad and (*b*) $\theta = 34$ mrad, respectively. For $\theta = 14$ mrad, the (10) rod is outside the Ewald sphere for the vacuum wave vector. The associated wave $\psi_G(z)$ is therefore an evanescent wave in the vacuum region. This rod is then a closed channel and no electron flux escapes into the vacuum *via* this (10) rod, as is clearly shown in Fig. 4(*a*). For $\theta = 34$ mrad, the (10) rod becomes an open channel and the electron wave associated with this rod is now a propagating wave and the intensity distribution is seen to be uniform in the region far from the surface in the vacuum. The electron penetration depth is also seen to depend sensitively on the angle of incidence, being a few atomic layers (Fig. 4*a*) or many layers (Fig. 4*b*).

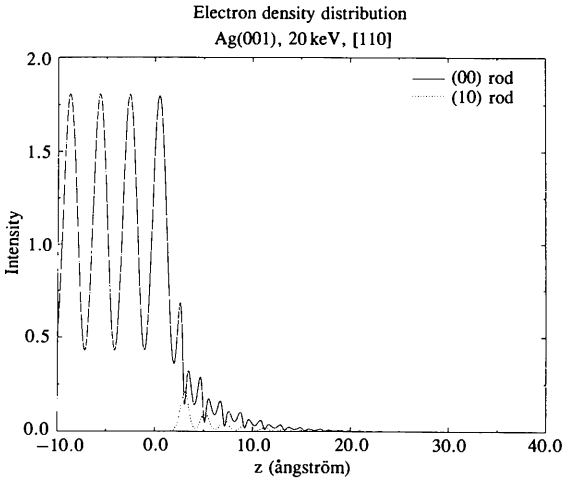

Fig. 4. Intensity distribution $|\psi_G(z)|^2$ for the (00) and (10) rods. The calculations are made for 20 keV incident-beam energy, an Ag(001) surface, the [110] beam azimuth and an angle of incidence θ of (*a*) 14.0 mrad and (*b*) 34.0 mrad.

5. Bethe potentials, evanescent waves and HOLZ effects

In the previous section, we have shown that, to achieve a convergent dynamical RHEED calculation, a large number of HOLZ rods need to be used, including evanescent beams such as those associated with the MHOLZs. The inclusion of evanescent beams is difficult, particularly for those with large negative values of Γ_G^2. The contributions from such beams are small, but they result in Bloch waves with approximate $\mathcal{K}$ values of $\pm i(|\Gamma_G)^2|^{1/2}$. From (15), it is clear that since the expression for $\psi_G(z)$ now includes exponential terms like $\exp[(|\Gamma_G^2|)^{1/2}t]$, any finite numerical error in the Bloch-wave excitation amplitude $\alpha^{(i)}$ and eigenvectors $C_G^{(i)}$ will be exponentially amplified, and this is the divergence problem encounted in RHEED theory (Zhao *et al.*, 1988). On the one hand, we know that the contributions from individual evanescent beams corresponding to large $|\Gamma_G|$ are small while, on the other hand, the collective contribution from all the evanescent waves and HOLZ rods is not negligible. The inclusion of evanescent beams with large $|\Gamma_G|$ values is difficult because it requires very small slice thickness and therefore much more computer time, as well as an increase in the matrix size consequent on the inclusion of weak beams.

In this section, we will show that the Bethe potentials provide an ideal way for dealing with the evanescent beams and HOLZ effects. The Bethe potentials were first introduced by Bethe (1928) in the two-beam case in order to take into account the effects of weak beams on the strong beams. Although this method has been successfully used in transmission electron diffraction (TED) for interpreting critical-voltage effects (Uyeda, 1968), and more recently for many-beam TED calculations (Zuo, 1993), its potential importance for dynamical RHEED calculations has not yet been fully realized. Recently, Ichimiya (1988) discussed qualitatively, using Bethe potential ideas, the effects of diffusely scattered beams and surface reflections on RHEED rocking curves. In this section, we re-derive the Bethe potentials and incorporate them into our two-dimensional Bloch-wave formulation. We show that they provide a convenient and powerful means for dealing with evanescent waves with large imaginary parts of the wave vector and much of the HOLZ effects.

We start our derivation of the Bethe potentials from the fundamental equation (8), changing the general suffixes G and H to J and L, in view of the specific use of G and H introduced below:

$$(\mathcal{K}^2 - \Gamma_J^2)C_J - \sum_{L \neq J} U_{J-L}(z)C_L = 0. \qquad (36)$$

Suppose we may separate the diffracted beams into two groups, namely a set of n strong beams $\{\mathbf{G}\}$ and a set of m weak beams $\{\mathbf{H}\}$. Explicitly, we can re-write the

above fundamental equation as

$$\begin{pmatrix} \mathcal{K}^2 - \Gamma_G^2 & -U_{G-G'} & \cdots & -U_{G-H} & -U_{G-H'} & \cdots \\ -U_{G'-G} & \mathcal{K}^2 - \Gamma_{G'}^2 & \cdots & -U_{G'-H} & -U_{G'-H'} & \cdots \\ \vdots & \vdots & \ddots & \vdots & \vdots & \ddots \\ -U_{H-G} & -U_{H-G'} & \cdots & \mathcal{K}^2 - \Gamma_H^2 & -U_{H-H'} & \cdots \\ -U_{H'-G} & -U_{H'-G'} & \cdots & -U_{H'-H} & \mathcal{K}^2 - \Gamma_{H'}^2 & \cdots \\ \vdots & \vdots & \ddots & \vdots & \vdots & \ddots \end{pmatrix} \times \begin{pmatrix} C_G \\ C_{G'} \\ \vdots \\ C_H \\ C_{H'} \\ \vdots \end{pmatrix} = 0. \tag{37}$$

Expanding the lower half of the equation, we obtain

$$\begin{pmatrix} C_H \\ C_{H'} \\ \vdots \end{pmatrix} = \begin{pmatrix} \mathcal{K}^2 - \Gamma_H^2 & -U_{H-H'} & \cdots \\ -U_{H'-H} & \mathcal{K}^2 - \Gamma_{H'}^2 & \cdots \\ \vdots & \vdots & \ddots \end{pmatrix}^{-1} \times \begin{pmatrix} U_{H-G} & U_{H-G'} & \cdots \\ U_{H'-G} & U_{H'-G'} & \cdots \\ \vdots & \vdots & \ddots \end{pmatrix} \begin{pmatrix} C_G \\ C_{G'} \\ \vdots \end{pmatrix}. \tag{38}$$

Suppose that the major features of the diffraction problem in the slice are determined by the Bloch waves associated with the set of strong beams, then for the set of weak beams we may make the following approximation in (8):

$$\mathcal{K}^2 - \Gamma_H^2 \simeq K_z^2 - \Gamma_H^2, \tag{39}$$

and this approximation is adequate either for large angles of incidence such that $\mathcal{K}_z = K_z$ or for beams with large values of Γ_H^2. Substituting (38) and (39) into (37), we obtain a matrix equation for the set of strong beams $\{\mathbf{G}\}$:

$$\begin{pmatrix} \mathcal{K}^2 - (\Gamma_G^2 + \Delta\Gamma_G^2) & -(U_{G-G'} + \Delta U_{GG'}) & \cdots \\ -(U_{G'-G} + \Delta U_{G'G}) & \mathcal{K}^2 - (\Gamma_{G'}^2 + \Delta\Gamma_{G'}^2) & \cdots \\ \vdots & \vdots & \ddots \end{pmatrix} \times \begin{pmatrix} C_G \\ C_{G'} \\ \vdots \end{pmatrix} = 0, \tag{40}$$

in which

$$\begin{pmatrix} \Delta\Gamma_G^2 & \Delta U_{GG'} & \cdots \\ \Delta U_{G'G} & \Delta\Gamma_{G'}^2 & \cdots \\ \vdots & \vdots & \ddots \end{pmatrix} = \begin{pmatrix} U_{G-H} & U_{G-H'} & \cdots \\ U_{G'-H} & U_{G'-H'} & \cdots \\ \vdots & \vdots & \ddots \end{pmatrix} \times \begin{pmatrix} K_z^2 - \Gamma_H^2 & -U_{H-H'} & \cdots \\ -U_{H'-H} & K_z^2 - \Gamma_{H'}^2 & \cdots \\ \vdots & \vdots & \ddots \end{pmatrix}^{-1} \times \begin{pmatrix} U_{H-G} & U_{H-G'} & \cdots \\ U_{H'-G} & U_{H'-G'} & \cdots \\ \vdots & \vdots & \ddots \end{pmatrix}. \tag{41}$$

For a dynamical RHEED calculation involving n strong beams and m weak beams, the original $(m + n) \times (m + n)$ matrix equation (37) is then reduced to an $n \times n$ matrix equation (40). The calculations of $\Delta\Gamma_G^2$ and $\Delta U_{GG'}$ involve the calculation of an $m \times m$ matrix inversion to (41).

Alternatively, we can rearrange (38) to give

$$\{C_H\} = (\mathbf{I} - \mathbf{U}_H)^{-1}\mathbf{U}_{HG}\{C_G\}, \tag{42}$$

in which the matrices $\mathbf{U}_H$ and $\mathbf{U}_{HG}$ are given by

$$\mathbf{U}_H = \begin{pmatrix} 0 & U_{H-H'}/(K_z^2 - \Gamma_H^2) & \cdots \\ U_{H'-H}/(K_z^2 - \Gamma_{H'}^2) & 0 & \cdots \\ \vdots & \vdots & \ddots \end{pmatrix} \tag{43}$$

and

$$\mathbf{U}_{HG} = \begin{pmatrix} U_{H-G}/(K_z^2 - \Gamma_H^2) & U_{H-G'}/(K_z^2 - \Gamma_H^2) & \cdots \\ U_{H'-G}/(K_z^2 - \Gamma_{H'}^2) & U_{H'-G'}/(K_z^2 - \Gamma_{H'}^2) & \cdots \\ \vdots & \vdots & \ddots \end{pmatrix}, \tag{44}$$

respectively. For a general matrix $\mathbf{U}$, we can always make a similarity transformation of the matrix

$$\mathbf{U} = \mathbf{\Gamma}\{\lambda_i\}_{\text{diag}}\mathbf{\Gamma}^{-1}, \tag{45}$$

in which $\{\lambda_i\}_{\text{diag}}$ is a diagonal matrix. Suppose, for all i, $\lambda_i \ll 1$, then we can use the approximation

$$(\mathbf{I} - \mathbf{U}_H)^{-1} = \mathbf{\Gamma}(\mathbf{I} - \{\lambda_i\}_H)^{-1}\mathbf{\Gamma}^{-1} \simeq \mathbf{I} \tag{46}$$

to obtain the well known expressions for the Bethe potentials (Bethe, 1928) in (40):

$$\begin{aligned} \Delta\Gamma_G^2 &= \sum_H |U_{G-H}|^2/(K_z^2 - \Gamma_H^2), \\ \Delta U_{GG'} &= \sum_H (U_{G-H}U_{H-G'})/(K_z^2 - \Gamma_H^2). \end{aligned} \tag{47}$$

The Bethe approximation (46) requires that

$$|K_z^2 - \Gamma_H^2| \gg |U_{G-H}| \tag{48}$$

for all weak beams $\{\mathbf{H}\}$ and all interactions between the weak beams and the strong beams $\{U_{G-H}\}$. Since K_z^2 is always positive, the inequality (48) clearly shows that the approximation is more likely to be valid for an evanescent beam for which $\Gamma_H^2 < 0$ than for a propagating beam with $\Gamma_H^2 > 0$.

If we have the further inequality that

$$|\Gamma_G^2| \gg K_z^2, \tag{49}$$

we then obtain

$$\begin{aligned} \Delta\Gamma_G^2 &\simeq -\sum_H (1/\Gamma_H^2)|U_{G-H}|^2, \\ \Delta U_{GG'} &\simeq -\sum_H (1/\Gamma_H^2) U_{G-H} U_{H-G'}, \end{aligned} \tag{50}$$

and this is the expression given by Beeby (1992). The Beeby approximation (49) is valid only for small angles of incidence, *i.e.* for small K_z. It is therefore more restricted than the Bethe approximation. The latter can be applied to the glancing-angle RHEED and large-angle TED diffraction geometries.

The domain of validity of the Bethe approximation (48) is shown schematically in Fig. 5. The quantity plotted in the figure is $S(H_x)$, given by

$$\begin{aligned} S(H_x) = \Gamma_H^2 - K_z^2 &= -H^2 - 2\mathbf{K}\cdot\mathbf{H} \\ &= -(2K_y H_y + H_y^2 + H_x^2), \end{aligned} \tag{51}$$

where the x axis is defined to be perpendicular to the incident beam and the y axis to be along the beam azimuth. For ZOLZ beams, we have $\mathbf{K}\cdot\mathbf{H} = 0$, for positive HOLZ beams $\mathbf{K}\cdot\mathbf{H} < 0$, and negative HOLZ beams $\mathbf{K}\cdot\mathbf{H} > 0$. The $S(H_x)$ curves associated with the positive HOLZ beams appear above the curve associated with the ZOLZ, and those associated with the minus HOLZ beams appear below the ZOLZ curve. The two solid horizontal lines in the figure divide the space into three regions. The regions above and below the lines approximately satisfy the Bethe approximation (48). The two dotted horizontal lines are boundaries of the Beeby approximation. The regions above and below these dotted lines approximately satisfy the Beeby approximation (49). Fig. 5 clearly shows that the domain of validity of the original Bethe approximation embraces that of the Beeby approximation, and in the present paper we will consider only the Bethe approximation.

Fig. 5 also shows that, for ZOLZ and MHOLZ beams, only a small number of low-order beams need to be treated fully. The higher-order beams lie below the lower solid line and can be treated approximately using the Bethe potentials. For HOLZ beams, the situation may be different. It is seen that while some low-order HOLZ beams with small values of H_x satisfy the Bethe approximation, some intermediate-order HOLZ beams need to be treated fully. It is also clear that the number of beams that need to be treated fully is smaller for MHOLZs than for HOLZs.

An alternative view of the domain of validity of the Bethe approximation is illustrated in Fig. 6. This figure shows the Laue circle (the intersection of the Ewald sphere made by the plane parallel to the crystal surface at the end of the wave vector of the incident beam) and the two-dimensional reciprocal lattice. We can re-write the quantity S as

$$S = \Gamma_H^2 - K_z^2 \simeq 2K_t(K_t - |\mathbf{K}_t + \mathbf{H}|). \tag{52}$$

In this expression, the radius of the Laue circle is given by K_t and the distance between the reciprocal-lattice rod $\mathbf{H}$ and the Laue circle is $K_t - |\mathbf{K}_t + \mathbf{H}|$. It should be noted that, to correct for the effect due to a 'weak beam' using the Bethe potentials, the ratio between U_{G-H} and $\Gamma_H^2 - K_z^2$ must be very small. Even though a beam may be very weak owing to the weakness of its interaction with all other beams (*i.e.* $U_{G-H} << U_G$), if the rod lies on or close to the Laue circle this beam cannot be treated as a weak beam by the method of Bethe potentials. The domain of validity of the Bethe approximation is given by the region outside the two concentric circles above and below the Laue circle.

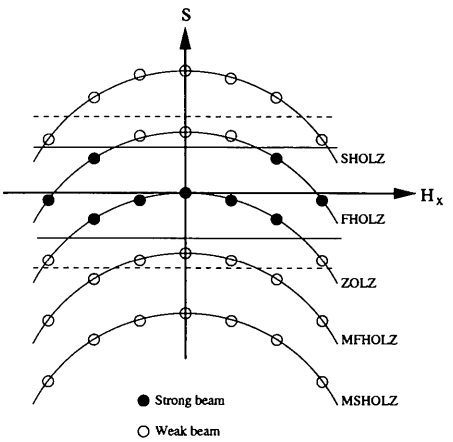

Fig. 5. Schematic diagram showing the domain of validity of the Bethe approximation.

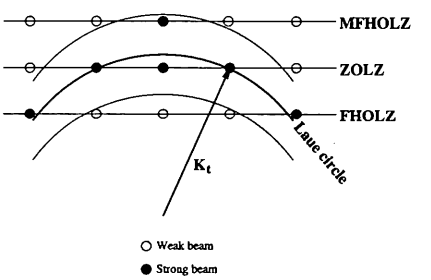

Fig. 6. An alternative view of the domain of validity of the Bethe approximation and the construction of the Laue circle on the xy plane.

Shown in Fig. 7 are the absolute beam amplitudes $|\mathcal{R}_G|$ for (*a*) (00) and (*b*) (10) rods. The three curves shown in this figure are calculated using 16 and 41 rods. The curve labelled '16rods + Bethe potentials' are calculated using 41 rods, but of these 41 rods only 9 ZOLZ rods and 7 first-order HOLZ rods are treated fully. Effects due to the remaining 25 weak beams are incorporated using the Bethe potentials. The 16 strong beams are $(0,0)$, $(\pm1,0)$, $(\pm2,0)$, $(\pm3,0)$, $(\pm4,0)$, $(-1,0)$, $(-1,\pm1)$, $(-1,\pm2)$, $(-1,\pm3)$, and the 25 weak beams are $(1,0)$, $(1,\pm1)$, $(1,\pm2)$, $(1,\pm3)$, $(\pm2,0)$, $(\pm2,\pm1)$, $(\pm2,\pm2)$, $(\pm3,0)$, $(\pm3,\pm1)$ and $(\pm4,0)$. This figure shows clearly that the Bethe potential method works almost perfectly in correcting for the effects of evanescent waves and HOLZ reflections.

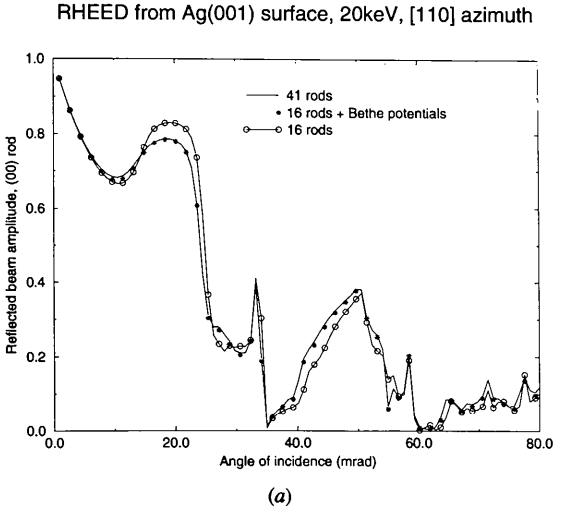

(*a*)

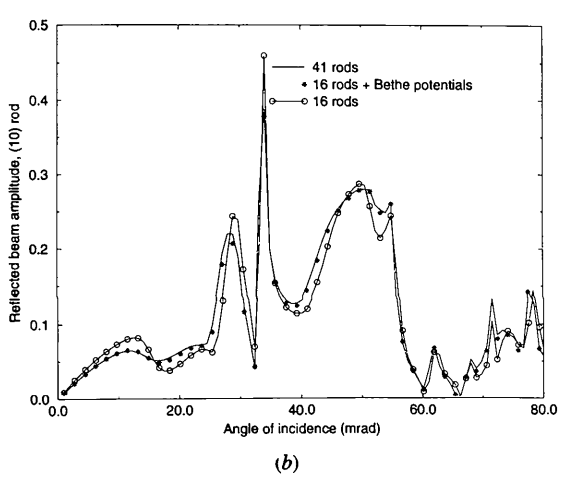

(*b*)

Fig. 7. Variation curves of $|\mathcal{R}_G|$ for (*a*) the (00) rod and (*b*) the (10) rod. Calculations in this figure are made for 20 keV incident-beam energy, an Ag(001) surface, the [110] beam azimuth, and using 16 rods, 41 rods, and the Bethe potentials for 16 strong beams and 25 weak HOLZ beams.

For a convergent calculation when many rods of the reciprocal lattice are involved, the procedure that is most computer time consuming is the diagonalization of the matrix equation (8). For a general $n \times n$ complex matrix, the time need to diagonalize the matrix is proportional to n^3. On the other hand, the calculation for the Bethe-potential method is proportional to n. Assuming that among the n rods m of them need to be treated fully, the computer time needed is proportional to m^3+n. The time saved by the use of the Bethe potentials is approximately proportional to $n^3 - m^3 - n$. It should be noted that this is only a rough estimate. The actual computer time used for the diagonalization of a matrix depends also on the detailed structure of the matrix.

6. RHEED from a reconstructed surface

In this section, we consider dynamical RHEED calculation from a reconstructed surface. In general, the two-dimensional rods of the reciprocal lattice in the plane parallel to the surface describing the periodicity of the substrate and the selvedge will not be identical. Since the structure of the substrate is often a known structure, it may then be used as the basis structure. In what follows, we shall use the set of reflections $\{\mathbf{G}\}$ to denote the substrate rods of the reciprocal lattice in the plane parallel to the surface and call it the fundamental set. The general set of surface rods $\{\mathbf{G}_s\}$ may be represented in terms of the fundamental set $\{\mathbf{G}\}$:

$$\{\mathbf{G}_s\} = \{\mathbf{G}, \mathbf{G} + \mathbf{s}_1, \ldots\}, \tag{53}$$

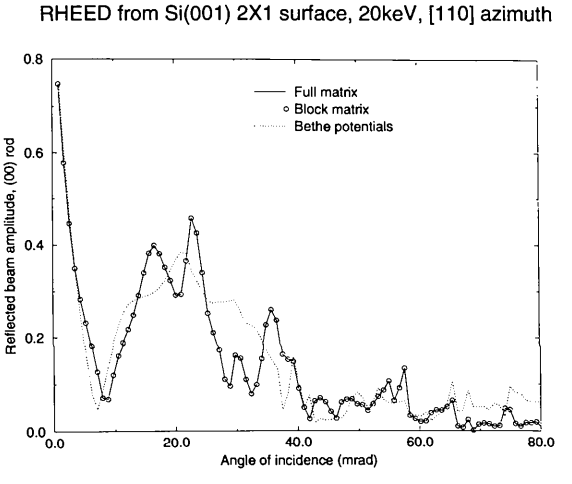

Fig. 8. Amplitudes of the specular beam reflected from an Si(001) 2 × 1 surface. 20 keV high-energy electrons are incident at the surface along the [110] azimuth. The three curves shown in this figure are calculated using 5 fundamental ZOLZ rods and 5 surface rods, based on a full scattering matrix **M**, a block scattering matrix **M′** and the Bethe potential method, treating the 5 fundamental rods as strong beams and the 5 surface rods as weak beams.

in which $\{\mathbf{s}_i\}$ is a set of surface rods lying within the first Brillouin zone of the fundamental rods.

We now consider the (001) surface of silicon as an example. After appropriate treatment in ultra-high vacuum, this surface reconstructs as a 2×1 structure in which the surface unit-cell edges are parallel to those in the (001) plane of the bulk silicon crystal, with the lattice parameters $\mathbf{a}_s = 2\mathbf{a}_b$, $\mathbf{b}_s = \mathbf{b}_b$. In reciprocal space, we have $\mathbf{a}_s^* = \mathbf{a}_b^*/2$, $\mathbf{b}_s^* = \mathbf{b}_b^*$. The complete set of surface reflections may then be written as $\mathbf{G}_s = \{\mathbf{G}, \mathbf{G} + \mathbf{a}_b^*/2, \mathbf{G} - \mathbf{a}_b^*/2\}$, *i.e.* $\mathbf{s}_1 = -\mathbf{s}_2 = \mathbf{a}_b^*/2$.

It is a general feature of surface reflections that in most cases they are relatively weak compared with fundamental reflections. It was therefore suggested by Ichimiya (1988) that effects from surface reflections could be discussed using Bethe potentials. Shown in Fig. 8 are three curves of $|\mathcal{R}_{00}|$ from the Si(001) 2×1 reconstructed surface for 20 keV and the [110] beam azimuth, using the Yin & Cohen (1981) model for the 2×1 reconstructed surface of silicon. The curve labelled 'full matrix' is calculated treating the ZOLZ rods fully, including the superlattice reflections. The curve labelled 'Bethe potentials' is calculated treating only the fundamental rods by the full-matrix method, the other surface rods being treated by Bethe potentials. This figure clearly shows that the method of Bethe potentials does not work well for ZOLZ surface reflections. This result is indeed expected because although the relevant Fourier coefficients U_{G+s_i} for surface reflections are relatively weak, the distances of many of the ZOLZ surface rods from the Laue circle are not large (Beeby, 1992). The Bethe-potentials method is therefore not well adapted for these reflections.

Although the Bethe potentials are not applicable for the many ZOLZ surface reflections, much of the computation of the substrate scattering is redundant and we shall now consider the substrate scattering in more detail. In the substrate, we have several groups of reflections (*e.g.* $\{\mathbf{G}\}$, $\{\mathbf{G} + s_1\}$, ...) propagating independently. This is because the coupling between these groups of reflections is zero in the substrate, *i.e.* $U_{G+s_i, G+s_j} = 0$ for all $i \neq j$. This characteristic feature of substrate diffraction may be explored more fully as has been done in the transmission geometry of electron diffraction (Peng & Whelan 1991).

The fundamental equation (8) can then be expressed in a block form:

$$\begin{pmatrix} \{A_0\} & 0 & \cdots \\ 0 & \{A_1\} & \cdots \\ \vdots & \vdots & \ddots \end{pmatrix} \begin{pmatrix} \{C_0\} \\ \{C_1\} \\ \vdots \end{pmatrix} = 0, \tag{54}$$

in which

$$\{A_0\}_{GH} = (K^2 - \Gamma_G^2)\delta_{GH} - U_{GH}(1 - \delta_{GH})$$
$$\vdots$$
$$\{A_i\}_{G+s_i, H+s_i} = (K^2 - \Gamma_{G+s_i}^2)\delta_{GH} - U_{GH}(1 - \delta_{GH})$$
$$\vdots$$

and

$$\{C_0\} = \begin{pmatrix} C_G \\ \vdots \\ C_H \\ \vdots \end{pmatrix}, \ldots, \{C_i\} = \begin{pmatrix} C_{G+s_i} \\ \vdots \\ C_{H+s_i} \\ \vdots \end{pmatrix}, \ldots. \tag{55}$$

Suppose now that we have a total of n fundamental reciprocal-lattice rods, then the matrix equation

$$\mathbf{A}_k \mathbf{C}_k = 0$$

gives n distinct eigenvalues $K_k^{2(i)}$, n eigenvectors $C_k^{(i)}$ ($i = 1, \ldots, n$) and $2n$ distinct Bloch waves. The complete eigenvectors can be constructed from these sub-eigenvectors as follows:

$$\begin{pmatrix} \{C_0^{(j)}\} \\ \{C_1^{(j)}\} \\ \vdots \end{pmatrix} = \begin{cases} \begin{pmatrix} \{C_0^{(i)}\} \\ \{0\} \\ \{0\} \\ \vdots \end{pmatrix} & \text{for } j = i = 1, \ldots, n \\ \begin{pmatrix} \{0\} \\ \{C_1^{(i)}\} \\ \{0\} \\ \vdots \end{pmatrix} & \text{for } j = i + n \\ & \quad = n + 1, \ldots, 2n \\ \vdots & \vdots \, . \end{cases} \tag{56}$$

The $\mathbf{C}$ matrix as defined in (18) now has the form

$$\mathbf{C} = \begin{pmatrix} \begin{Bmatrix} \{C_0^{(i)}\} & 0 & \cdots \\ 0 & \{C_1^{(i)}\} & \cdots \\ \vdots & \vdots & \ddots \end{Bmatrix} & \begin{Bmatrix} \{C_0^{(i)}\} & 0 & \cdots \\ 0 & \{C_1^{(i)}\} & \cdots \\ \vdots & \vdots & \ddots \end{Bmatrix} \\ \begin{Bmatrix} \{K_0^{(i)} C_0^{(i)}\} & 0 & \cdots \\ 0 & \{K_1^{(i)} C_1^{(i)}\} & \cdots \\ \vdots & \vdots & \ddots \end{Bmatrix} & \begin{Bmatrix} \{-K_0^{(i)} C_0^{(i)}\} & 0 & \cdots \\ 0 & \{-K_1^{(i)} C_1^{(i)}\} & \cdots \\ \vdots & \vdots & \ddots \end{Bmatrix} \end{pmatrix}. \tag{57}$$

If we re-write the vector Ψ as

$$\Psi' = \begin{pmatrix} \{\psi_0\} \\ \{\psi_1\} \\ \vdots \end{pmatrix}, \tag{58}$$

the total scattering matrix then has a block form:

$$\mathbf{M}' = \begin{pmatrix} \{M_0\} & & \\ & \{M_1\} & \\ & & \ddots \end{pmatrix}, \tag{59}$$

$$\mathbf{M}(t) = \mathbf{C}\Upsilon\mathbf{C}^{-1} = \begin{pmatrix} \left\{\sum_i C_G^{(i)} \cos \mathcal{K}^{(i)} t \; C_H^{*(i)}\right\} & \left\{i \sum_i C_G^{(i)} \sin \mathcal{K}^{(i)} t \; C_H^{*(i)}/\mathcal{K}^{(i)}\right\} \\ \left\{i \sum_i \mathcal{K}^{(i)} C_G^{(i)} \sin \mathcal{K}^{(i)} t \; C_H^{*(i)}\right\} & \left\{\sum_i C_G^{(i)} \cos \mathcal{K}^{(i)} t \; C_H^{*(i)}\right\} \end{pmatrix}. \tag{62}$$

in which

$$\{M_k\} = \begin{pmatrix} \{C_k^{(i)}\} & \{C_k^{(i)}\} \\ \{\mathcal{K}_k^{(i)} C_k^{(i)}\} & \{-\mathcal{K}_k^{(i)} C_k^{(i)}\} \end{pmatrix} \times \begin{pmatrix} \{\exp(i\mathcal{K}_k^{(i)} t)\} & \{0\} \\ \{0\} & \{\exp(-i\mathcal{K}_k^{(i)} t)\} \end{pmatrix} \times \begin{pmatrix} \{C_k^{(i)}\} & \{C_k^{(i)}\} \\ \{\mathcal{K}_k^{(i)} C_k^{(i)}\} & \{-\mathcal{K}_k^{(i)} C_k^{(i)}\} \end{pmatrix}^{-1}. \tag{60}$$

It should be noted that the vector Ψ' and scattering matrix $\mathbf{M}'$ as defined here differ from those defined in (17) only in indexing notation, and they can easily be transformed to the form defined in (17). The points in Fig. 8 denoted by circles have been calculated using the block scattering matrix $\mathbf{M}'$. These points are seen to coincide with the curve calculated using the full scattering matrix $\mathbf{M}$. Suppose we have a total of n fundamental rods and m sets of surface reflections. Then the computer time for calculations based on the full scattering matrix $\mathbf{M}$ will be roughly proportional to $(nm)^3$. On the other hand, if the block form of the scattering matrix $\mathbf{M}'$ is used, the computation time will scale as $m \times n^3$. When m is large, such as for the Si(111) 7×7 surface, the saving in computer time will be substantial.

7. Perturbation treatment of the anomalous absorption effect

For purely elastic RHEED, the electrostatic potential $U(\mathbf{R}, z)$ is real. From the fitting parameters a_j, b_j as given by Doyle & Turner (1968), an analytical expression for $U_G(z)$ can be obtained [see for example Appendix B of Peng (1994)], and for a real potential $U_{-G}(z) = U_G^*(z)$. For a thin slice the matrix associated with the eigenvalue equation (8),

$$\{A\}_{GH} = \Gamma_G^2 \delta_{GH} + U_{GH}(1 - \delta_{GH}),$$

is Hermitian. The associated eigenvectors then satisfy the following orthogonal relations:

$$\sum_i C_G^{*(i)} C_H^{(i)} = \delta_{GH}, \qquad \sum_G C_G^{*(i)} C_G^{(j)} = \delta_{ij}. \tag{61}$$

An analytical expression for the scattering matrix defined in (21) can be obtained (Peng & Whelan, 1990):

For RHEED from the surface of an absorbing crystal, the optical potential becomes complex, *i.e.* $U_G(z)$ in the non-absorbing case is replaced by $U_G(z) + iU'_G(z)$. We assume first that the absorption is dependent on z only, *i.e.* $U'_G(z) = 0$ for all $G \neq 0$. The inclusion of the mean absorption $iU'_0(z)$ in the eigenvalue equation (8) then introduces only a shift to the eigenvalues and the eigenvectors remain unchanged. Assuming that $\mathcal{K}^{(i)2}$ are solutions of (8) for elastic RHEED, we then have

$$\mathcal{K}'^{(i)2} = \mathcal{K}^{(i)2} + iU'_0(z), \tag{63}$$

when $iU'_0(z)$ is incorporated in (8).

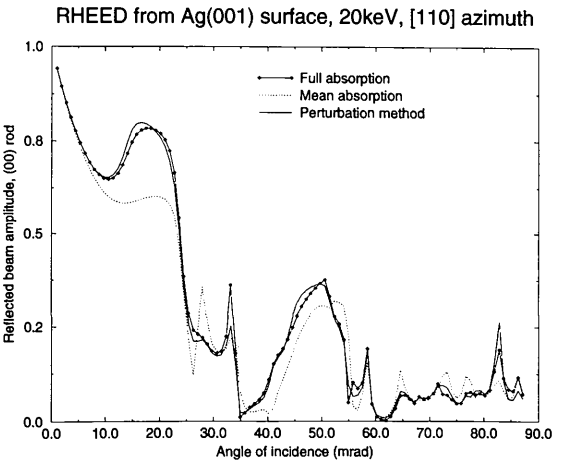

Fig. 9. Amplitudes of the specular beam reflected from an Ag(001) surface. The incident-beam energy is 20 keV and the beam azimuth is along the [110] direction. The three curves in the figure are calculated using the full dynamical theory (labelled 'full absorption'), the mean absorption model (labelled 'mean absorption') and the perturbation method (labelled 'perturbation method').

Shown in Fig. 9 are three curves calculated using the general absorption model as discussed in §3 (labelled 'full absorption'), the mean absorption model (labelled 'mean absorption') and the perturbation method (labelled 'perturbation method'), which we will discuss below. The anomalous absorption effect resulting from iU'_G on the RHEED rocking curve is noticeable.

While the anomalous absorption effect is not negligible, it is generally true that $U'_G \ll U_G$. This fact suggests that the anomalous effect may be treated using a perturbation method such as has been successfully applied in the transmission (THEED) case (Hirsch, Howie, Nicholson, Pashley & Whelan, 1965). To a first-order approximation, we assume that the inclusion of $U'_G(z)$ in the eigenvalue equation (8) does not change the eigenvectors appreciably. Letting

$$K'^{(i)2} = K^{(i)2} + \Delta K^{(i)2},$$

we have from (8)

$$\Delta K^{(i)2} C_G^{(i)} + (K^{(i)2} - \Gamma_G^2 - iU'_0) C_G^{(i)} - \sum_{H \neq G} U_{G-H} C_H^{(i)} - i \sum_{H \neq G} U'_{G-H} C_H^{(i)} = 0.$$

Pre-multiplying this equation by $C_G^{*(i)}$, summing over all **G** and using the orthogonality relations (61) and equation (8), we then obtain

$$\Delta K^{(i)2} = i \sum_G C_G^{*(i)} U'_{G-H}(z) C_H^{(i)}. \quad (64)$$

The third rocking curve in Fig. 9, labelled 'perturbation method', is calculated using (62) but with modified eigenvalues calculated using (64):

$$K'^{(i)} = [K^{(i)2} + \Delta K^{(i)2}]^{1/2}. \quad (65)$$

It is seen that the perturbation method works reasonably well for this particular case but there exist some noticeable discrepancies. In principle, the accuracy of the perturbation method may be improved by including not only the perturbation of the eigenvalues but also of the eigenvectors and by including higher-order terms. However, calculation of these corrections demands more computer time than that required using full dynamical theory. It is therefore numerically inefficient to use higher-order terms in dynamical electron diffraction calculations, except when it is intended to invert the structure directly from a reference structure (Peng & Dudarev, 1993*a*,*b*).

8. Conclusions

Dynamical RHEED calculations have been made using two-dimensional Bloch waves. This approach is applicable to a general complex optical potential. It is found that to achieve a convergent result many rods of the reciprocal lattice, including those that lie outside the Ewald sphere (*i.e.* those giving rise to evanescent waves) need to be included and HOLZ effects are not always negligible.

The Bethe potentials have been incorporated into our two-dimensional Bloch-wave formulation. We have shown that the use of the Bethe potentials is very efficient in dealing with HOLZ and evanescent rods that lie far away from the Laue circle, and that the saving in the computer time is typically more than 15 times.

For RHEED from a reconstructed surface, we have shown that the Bethe potential method is not always applicable for dealing with weak surface reflections lying on the ZOLZ. To reduce the amount of computation, a new method has been developed utilizing the block structure of the scattering matrix of the substrate. The results obtained using this new scheme are identical to those obtained using full dynamical RHEED theory. The computation efficiency is improved by about 40 to 60%.

The anomalous absorption effect has been shown to be important in RHEED. Standard perturbation theory has been applied to correct for this effect. It is found that in general this perturbation method works reasonably well but does not have high accuracy. The computation speed is increased by about 30%.

This work was supported by the Chinese Academy of Sciences and National Natural Science Foundation of China (LMP), by the Engineering and Physical Science Research Council of the UK (grant nos. GR/H96423 and GR/H58278) and by the Royal Society (Joint Project no. Q711).

References

Beeby, J. L. (1992). *Appl. Surf. Sci.* **60/61**, 405–410.
Bethe, H. (1928). *Ann. Phys. (Leipzig)*, **87**, 55–69.
Bird, D. M. & King, Q. A. (1990). *Acta Cryst.* A**46**, 202–208.
Cohen, P. I. & Ichimiya, A. (1993). Editors. *Proceedings of US–Japan Seminar on Surface Characterization by Electron Diffraction, REM, and Holography. Surf. Sci.* **298**.
Doyle, P. A. & Turner, P. S. (1968). *Acta Cryst.* A**24**, 390–397.
Dudarev, S. L., Peng, L.-M. & Whelan, M. J. (1995). *Surf. Sci.* **330**, 86–100.
Dudarev, S. L. & Whelan, M. J. (1994). *Surf. Sci.* **310**, 373–389.
Hall, C. R. & Hirsch, P. B. (1965). *Proc. R. Soc. London Ser. A*, **286**, 158–177.
Hirsch, P. B., Howie, A., Nicholson, R. B., Pashley, D. W. & Whelan, M. J. (1965). *Electron Microscopy of Thin Crystals.* London: Butterworths.
Ichimiya, A. (1983) *Jpn. J. Appl. Phys.* **22**, 176–180.
Ichimiya, A. (1988). *Acta Cryst.* A**44**, 1042–1044.
Ichimiya, A. (1996). *Winter Workshop on Electron Diffraction and Imaging at Surfaces*, January 1996, Scottsdale, Arizona, USA.
Larsen, P. K. & Dobson, P. J. (1988). Editors. *RHEED and Reflection Electron Imaging of Surfaces.* New York: Plenum.

Lynch, D. F. & Moodie, A. F. (1972). *Surf. Sci.* **32**, 422–438.
Maksym, P. A. & Beeby, J. L. (1981). *Surf. Sci.* **110**, 423–438.
Meyer-Ehmsen, G. (1989). *Surf. Sci.* **219**, 177–188.
Pendry, J. (1974). *Low Energy Electron Diffraction*. New York: Academic Press.
Peng, L.-M. (1994). *Advances in Imaging and Electron Physics*, edited by P. W. Hawkes, Vol. 90, pp. 205–351. New York: Academic Press.
Peng, L.-M. & Cowley, J. M. (1986). *Acta Cryst.* A**42**, 545–552.
Peng, L.-M. & Cowley, J. M. (1988). *Surf. Sci.* **199**, 609–622.
Peng, L.-M. & Dudarev, S. L. (1993*a*). *Ultramicroscopy*, **52**, 312–317.
Peng, L.-M. & Dudarev, S. L. (1993*b*). *Surf. Sci.* **298**, 316–330.
Peng, L.-M., Dudarev, S. L. & Whelan, M. J. (1996). *Acta Cryst.* A**52**, 471–475.
Peng, L.-M., Ren, G., Dudarev, S. L. & Whelan, M. J. (1996*a*). *Acta Cryst.* A**52**, 257–276.
Peng, L.-M., Ren, G., Dudarev, S. L. & Whelan, M. J. (1996*b*). *Acta Cryst.* A**52**, 456–470
Peng, L.-M. & Whelan, M. J. (1990). *Proc. R. Soc. London Ser. A*, **431**, 111–124, 125–142.
Peng, L.-M. & Whelan, M. J. (1991). *Acta Cryst.* A**47**, 101–109.
Radi, G. (1970). *Acta Cryst.* A**26**, 41–56.
Smith, A. E. & Lynch, D. F. (1988). *Acta Cryst.* A**44**, 780–788.
Sturkey, L. (1962). *Proc. Phys. Soc.* **80**, 321–354.
Tournarie, M. (1962). *J. Phys. Soc. Jpn*, **17**, Suppl. BII, 98–100.
Uyeda, R. (1968). *Acta Cryst.* A**24**, 175–181.
Whelan, M. J. (1965*a*). *J. Appl. Phys.* **36**, 2099–2103.
Whelan, M. J. (1965*b*). *J. Appl. Phys.* **36**, 2104–2110.
Yin, M. T. & Cohen, M. L. (1981). *Phys. Rev. B*, **24**, 2303–2306.
Yoshioka, H. (1957) *J. Phys. Soc. Jpn*, **12**, 618–628.
Yoshioka, H. & Kainuma, Y. (1962). *J. Phys. Soc. Jpn*, **17**, Suppl. BII, 141–145.
Zhao, T. C., Poon, H. C. & Tong, S. Y. (1988). *Phys. Rev. B*, **38**, 1172–1195.
Zhao, T. C. & Tong, S. Y. (1988). *Ultramicroscopy*, **26**, 151–160.
Zuo, J. M. (1993). *Acta Cryst.* A**49**, 429–435.